Chinese Chemical Letters 37 (2026) 111541

Contents lists available at ScienceDirect

Chinese Chemical Letters

journal homepage: www.elsevier.com/locate/cclet

Aptamer-targeted and pH-responsive DNA tetrahedron for survivin mRNA fluorescence imaging and chemo/gene therapy

Mengyue Li[a,b], Yue Zheng[a], Zhijun Lu[a], Yu Yang[a], Jiangping Lei[a], Yi Teng[a], Wanyi Zhou[a], Yiman Ge[c], Chunhui Wu[a], Hong Yang[a,*], Yiyao Liu[a,c,d,e,*]

[a] Sichuan Clinical Research Center for Cancer, Sichuan Cancer Hospital & Institute, Sichuan Cancer Center, and School of Life Science and Technology, University of Electronic Science and Technology of China, Chengdu 610041, China
[b] Institute for Engineering Medicine, Kunming Medical University, Kunming 650500, China
[c] Department of Otorhinolaryngology, Hospital of Chengdu University of Traditional Chinese Medicine, Chengdu 610072, China
[d] Traditional Chinese Medicine (TCM) Regulating Metabolic Diseases Key Laboratory of Sichuan Province, Hospital of Chengdu University of Traditional Chinese Medicine, Chengdu 610072, China
[e] Department of Urology, Deyang People's Hospital, Deyang 618099, China

ARTICLE INFO

Article history:
Received 10 April 2025
Revised 30 June 2025
Accepted 2 July 2025
Available online 6 July 2025

Keywords:
Dynamic DNA nanostructures
DNA tetrahedrons
Survivin mRNA imaging
Chemo/gene therapy
Targeted delivery

ABSTRACT

In situ stimuli-responsive nanodevices have gained substantial attention in recent years owing to their remarkable potential to enhance tumor imaging and therapeutic effects. Herein, we formulated a pH-responsive, aptamer-functionalized DNA tetrahedral nanoplatform (ASTD) for improved visualization of survivin mRNA and chemo/gene therapy. ASTD, assembled by four single-stranded DNA, integrates pH-responsive i-motif sequences, survivin mRNA-targeted molecular beacons and AS1411 aptamers. Taking advantage of the tumor-targeting ability of AS1411 aptamer, ASTD monomers self-assemble into a multifunctional DNA polymeric tetrahedron (ASPD) on the tumor cell surface upon exposure to acidic tumor microenvironment. ASPD exhibits enhanced cellular uptake, superior survivin mRNA imaging, and efficient survivin gene silencing. Furthermore, Dox-loaded ASPD shows a significant antitumor effect, resulting in approximately 66 % apoptosis of tumor cells. This study develops a dynamic DNA tetrahedral nanoplatform with diagnostic and therapeutic dual-functionalities, offering a promising strategy for advancing precise cancer theranostics.

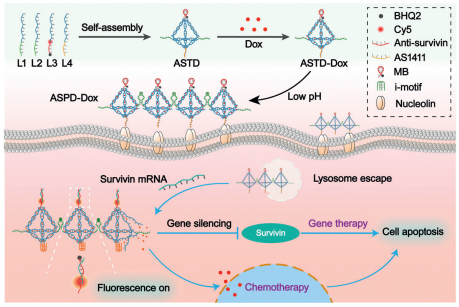
© 2026 Published by Elsevier B.V. on behalf of Chinese Chemical Society and Institute of Materia Medica, Chinese Academy of Medical Sciences.

Over the past few decades, integrating cancer diagnosis and therapy within a single drug delivery platform has been applied as a transformative approach in the precision medicine of cancer [1,2]. Theranostics enables personalized cancer treatment by using targeted imaging agents to identify tumors and simultaneously delivering therapeutic drugs. It streamlines clinical workflows while improving treatment accuracy compared to conventional sequential strategies [3,4]. Molecular beacons (MBs), as a powerful theranostic tool, have gained wide attention in cancer research due to their role in early detection, imaging, and targeted therapy [5–7]. MBs are hairpin-shaped nucleic acid probes that can be labeled by fluorescent tags. The fluorescent tags remain quenched and will recover fluorescence once they hybridize with complementary target mRNA sequences [8,9]. Therefore, MBs are highly sensitive to detecting cancer biomarkers and meanwhile perform the function of gene silencing [10,11]. One of the promising cancer biomarkers is survivin. It is highly expressed in most cancers including lung, breast, colorectal, pancreatic, and brain cancer, but almost absent in normal adult tissues [12,13]. This makes survivin a valuable tumor-specific marker for cancer diagnosis. Moreover, survivin is involved in tumor growth, proliferation, and apoptosis evasion [14]. Therefore, it is also an attractive potential candidate for anti-cancer treatments.

Given that the application of MBs is mainly limited by inefficient targeted delivery and cellular uptake, a critical challenge is to design a dual-functional nanoplatform, simultaneously sensing tumor biomarkers and delivering therapeutic medicine. DNA nanostructures have received extensive attention as delivery nanoplatforms for theranostics in recent years owing to their excellent biocompatibility and unparalleled ability to incorporate nucleic acids through complementary base pairing [15–18]. Moreover, DNA nanostructures can efficiently deliver the chemotherapeutic drug doxorubicin (Dox) [19–21]. As a classic anthracycline antibiotic, Dox intercalates into the molecules between the planar bases of

* Corresponding authors.
E-mail addresses: yanghongyh@uestc.edu.cn (H. Yang), liuyiyao@uestc.edu.cn (Y. Liu).

https://doi.org/10.1016/j.cclet.2025.111541
1001-8417/© 2026 Published by Elsevier B.V. on behalf of Chinese Chemical Society and Institute of Materia Medica, Chinese Academy of Medical Sciences.



Scheme 1. Schematic illustration of aptamer-targeted and acid-driven *in situ* assembly of DNA polymeric tetrahedron for potentiated survivin mRNA fluorescence imaging and chemo/gene therapy.

DNA. Among various DNA nanostructures, DNA tetrahedron (TD) is widely utilized for delivering drugs and functional oligos due to its efficient self-assembly, rigid framework, and symmetric three-dimensional structure [22–24]. However, certain limitations of TD still need to be addressed. Aptamers have been incorporated into TD to improve its tumor-targeting efficiency [25,26]. Aptamers are single-stranded nucleic acid ligands binding to a wide range of target molecules with high affinity and specificity. For example, AS1411 aptamer has a strong affinity to nucleolin highly expressed in breast cancer cells. Loading AS1411 aptamer in TD can significantly enhance its tumor-targeting ability [22,27,28]. Furthermore, dynamic stimuli-responsive assembly strategies have gained widespread interest in improving TD's internalization and accumulation efficiency and amplifying imaging signals [29–31]. Considering the acidic tumor microenvironment (TME), pH-sensitive DNA i-motif which undergoes a sharp structural transition from a random coil to a quadruplex at acidic conditions is employed to construct *in situ* stimuli-responsive nanostructures [32–34]. Motivated by these advances, integrating TDs with aptamers and pH-responsive i-motifs can facilitate cancer theranostics.

In this work, we fabricated a pH-responsive DNA tetrahedron (ASTD) that integrates AS1411 aptamer, survivin-targeted MB, and pH-responsive i-motif sequence. As shown in Scheme 1, four functionalized DNA strands were designed to construct ASTD, and then the chemotherapeutic drug Dox was intercalated to form ASTD-Dox. ASTD-Dox maintained monomeric dispersion at physiological pH and activated a dual-functional mechanism upon encountering tumor cells. AS1411 aptamer specifically targeted nucleolin, which is abundantly expressed and localized at the surface of cancer cells. Meanwhile, the acidic tumor environment triggered the reconstitution of two split i-motif DNA strands from different ASTD-Dox to form hand-in-hand DNA polymeric tetrahedrons (ASPD-Dox). This pH-triggered assembly of ASPD-Dox resulted in increased size, improved affinity, and enhanced cellular uptake. After the cellular internalization of ASPD-Dox, the survivin-targeted MB hybridized with survivin mRNA to silence survivin expression, and unfasten the MB's stem-loop structure. Unlocked MB restored fluorescence for real-time imaging of survivin mRNA. Survivin silencing and released Dox achieved combinative chemo/gene cancer therapy. In summary, ASTD as a stimuli-responsive DNA theranostic nanoplatform exhibits great potential for integrated diagnosis and precision therapy applications.

The successful assembly and pH-responsive behavior of ASTD were systematically characterized. The monomer was constructed by annealing four DNA single strands (L1–L4), and each strand was modified with distinct functional elements. Strands of L1 and L2 contain two split i-motif sequences that pair together to form a complete i-motif by pH-driven aggregation. L3 contains a MB labeled with Cy5/BHQ2 for survivin mRNA visualizing and silencing. L4 has an AS1411 aptamer for targeting tumor cells. Agarose gel

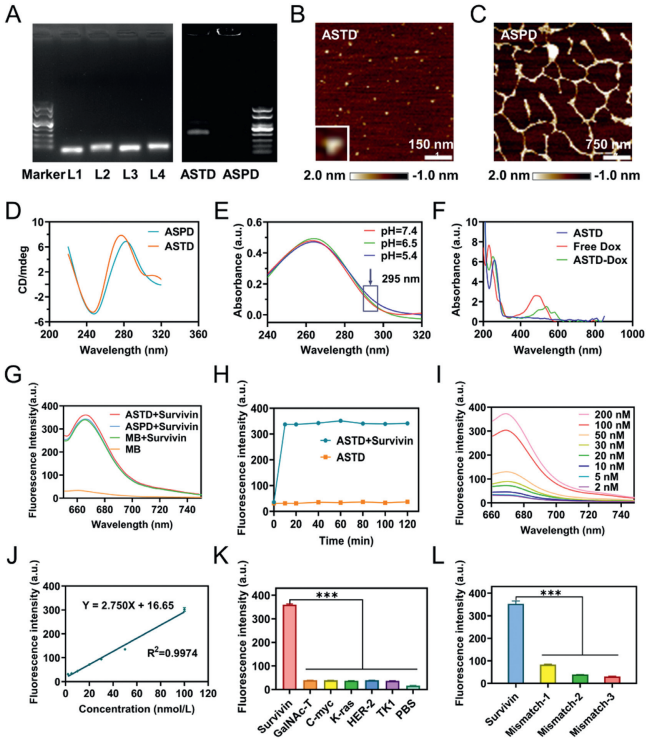


Fig. 1. Characterization of the TD-based tumor theranostic nanosystem and detection performance of DNA tetrahedral *in vitro*. (A) 2 % agarose gel electrophoresis analysis of the ASTD under pH 7.4 and the pH-driven ASPD under pH 6.5. AFM images of (B) ASTD, and (C) ASPD. Scale bar: 150 nm and 750 nm. (D) CD spectra characterization of the feasibility of the pH-driven DNA polymeric tetrahedron assembly under different pH values. (E) Verification of the formation of i-motif structure in ASTD (500 nmol/L) under different pH conditions (pH 5.4, 6.5, and 7.4) by UV absorption spectra. (F) UV–vis-NIR spectra of ASTD, Free Dox, and ASTD-Dox, respectively. (G) Feasibility of survivin target activation before and after assembly at 37 °C. Probe concentration: 200 nmol/L; MB concentration: 200 nmol/L. (H) Time-dependent fluorescence recovery of ASTD alone or addition of DNA target (survivin) (200 nmol/L) at 37 °C. (I) Fluorescence responses of the ASTD to the different concentrations of the DNA target (survivin mRNA) from 2 nmol/L to 200 nmol/L at 37 °C. nM = nmol/L. (J) The linear relationship between the fluorescence intensity and the concentration of the DNA target. (K) Fluorescence emission intensity of ASTD to several DNA targets (1. survivin target, 2. GalNAc-T target, 3. C-myc target, 4. K-ras target, 5. HER-2 target, 6. TK1 target, 7. PBS) at the same concentration (200 nmol/L). (L) Fluorescence emission intensity of ASTD under different numbers of mismatched bases of survivin mRNA analogs. Data are presented as the mean ± SD ($n = 3$). $^{***}P < 0.001$.

electrophoresis was performed to investigate the self-assembly of ASTD and the pH-triggered transition to ASPD. As shown in Fig. 1A, the successfully assembled ASTD migrated more slowly than the individual ssDNA strands, while the supramolecular ASPD was retained in the gel pores. AFM imaging further revealed the morphological changes from monomeric ASTD to polymeric ASPD (Figs. 1B and C). The formation of the polymeric structure and significantly increased size caused the retention of ASPD in agarose gel. Circular dichroism (CD) spectrophotometry showed that ASTD had a positive peak at 275 nm and a negative peak at 245 nm, which red-shifted to 285 and 250 nm (Fig. 1D), indicating the formation of intact intermolecular i-motifs under acidic conditions. Furthermore, ultraviolet (UV) absorption at 295 nm progressively increased as the pH decreased from 7.4 to 5.6 (Fig. 1E), consistent with the formation of intact i-motif structures as previously reported [35]. These results demonstrated the successful construction of ASTD and the pH-driven ASPD assembly under acidic conditions.

To enhance therapeutic efficacy, Dox was intercalated into ASTD to form ASTD-Dox. The UV–vis-NIR spectra showed a characteristic absorption peak at 510 nm for ASTD-Dox, distinct from that of Dox

at 480 nm. The red-shifted absorption peak of ASTD-Dox suggested the successful loading of Dox into ASTD (Fig. 1F). Then, the encapsulation efficiency of Dox was calculated (Fig. S1 in Supporting information). The concentration of ASTD was set at 200 nmol/L, and the ratio of ASTD to Dox was tested at a range of 1:50 to 1:300. After balancing the encapsulation efficiency and utilization rate of Dox, the ratio of 1:200 with an encapsulation efficiency of 75.43 % was selected for subsequent experiments.

The specificity and sensitivity of ASTD in detecting survivin mRNA highlight its potential as a reliable diagnostic tool, paving the way for further exploring its intracellular performance. To detect survivin mRNA by fluorescent visualization, the MB in ASTD was labeled with the fluorophore Cy5, and its fluorescence was quenched by the quencher BHQ2. The stem-loop MB can recognize and hybridize with survivin mRNA to form stable duplexes, resulting in the structural rearrangement and fluorescence recovery of Cy5. The ability of ASTD to detect survivin mRNA was examined at 37 °C. As shown in Fig. 1G, the MB, ASTD, and ASPD exhibited almost similar fluorescence recovery when exposed to survivin mRNA for the cell-free test. Next, the time-dependent study of ASTD fluorescence recovery revealed that ASTD rapidly responded to survivin mRNA and reached the maximum recovered fluorescence within 10 min (Fig. 1H). To further investigate the ASTD's responsiveness to different concentrations of survivin mRNA, we examined the concentrations of survivin mRNA ranging from 2 nmol/L to 200 nmol/L. A linear relationship between fluorescence intensity and survivin mRNA concentration was observed (Figs. 1I and J), indicating that ASTD can effectively detect different concentrations of survivin mRNA.

Achieving a reliable sequence-specific distinction among homologous transcripts is essential to utilize mRNA as a diagnostic biomarker. To assess the specificity of ASTD, survivin mRNA and diverse cellular mRNAs of GalNAc-T, C-myc target, K-ras, human epidermal growth factor receptor 2 (HER-2), and thymidine kinase 1 (TK1) were tested at an equivalent molar concentration. The fluorescence intensity responding to survivin mRNA was remarkably higher than that of non-target mRNAs (Fig. 1K and Fig. S2 in Supporting information). Then, the specificity of ASTD was further evaluated on modified survivin mRNAs with mismatched 1, 2, or 3 bases. The results showed that even one base mismatch significantly reduced the fluorescence recovery of ASTD (Fig. 1L and Fig. S3 in Supporting information). These results demonstrated that ASTD can specifically recognize survivin mRNA and effectively monitor its concentration by fluorescence recovery.

A typical hallmark of cancer is the acidic TME. Upon exposure to the acidic extracellular environment, ASTD will assemble into hand-in-hand DNA polymeric tetrahedrons (ASPD) by the reconstitution of split i-motif DNA strands. Given that efficient cellular uptake is a critical step in performing functions, we incubated MDA-MB-231 breast cancer cells with ASTD under different pH conditions to test if the dynamic stimuli-responsive assembly of ASPD improves cellular internalization and amplifies imaging signal. Both confocal imaging and flow cytometry results showed that the recovered fluorescence signal of Cy5 in MDA-MB-231 cells increased as extracellular pH decreased from 7.4 to 5.6 (Figs. S4A–C in Supporting information), suggesting that the pH-driven assembly of ASPD enhanced its cellular internalization. Subsequently, the MB, ASTD, and ASPD were incubated with MDA-MB-231 cells for 4 h at 37 °C to compare their cellular uptake efficiency. Confocal imaging results revealed that the recovered Cy5 fluorescence signal in the ASPD group was remarkably stronger than that in the ASTD group, and the MB group showed negligible fluorescence, consistent with the flow cytometry results (Figs. S5A–C in Supporting information). These results further demonstrated that the significantly improved cellular uptake efficiency is based on the formation of ASPD.

We subsequently assessed if the efficient cellular uptake of ASPD by tumor cells is also mediated by AS1411 aptamer. The MB labeled with only Cy5 instead of Cy5/BHQ2 was employed to construct ASPD-Cy5, the fluorescence of which can be excited directly without binding to target mRNAs for recovery. The MDA-MB-231 breast cancer cells incubated with ASPD-Cy5 (+AS1411 aptamer) exhibited much stronger fluorescence intensity of Cy5 than that incubated with SPD-Cy5 (-AS1411 aptamer) after 4 h, and also stronger than that of ASPD-Cy5 treated normal MCF-10A cells without membrane nucleolin (Fig. 2A). These results indicate that AS1411 aptamer significantly improved the tumor-targeted ability of ASPD and enhanced its cellular internalization. Next, we examined the endolysosomal escape capability of ASPD-Cy5 by using LysoTracker, a lysosomal marker in viable cells, to visualize its subcellular localization. The Cy5 signal overlapped with the LysoTracker signal after 2 h of incubation of MDA-MB-231 cells with ASPD-Cy5. However, the overlap of signals diverged after 6 h (Figs. 2B–D), indicating the endolysosomal release of ASPD-Cy5 into the cytoplasm of tumor cells.

After demonstrating ASPD's enhanced tumor targeting and cellular uptake, we next evaluated its ability to image endogenous survivin mRNA for precise cancer diagnosis. The real-time monitoring of endogenous survivin mRNA is a valuable method of cancer diagnosis. Therefore, we incubated MDA-MB-231 cells with ASPD to explore the ability of ASPD to visualize cytoplasmic survivin mRNA. As shown in Fig. S6 (Supporting information), the Cy5 fluorescence in MDA-MB-231 cells showed a time-dependent

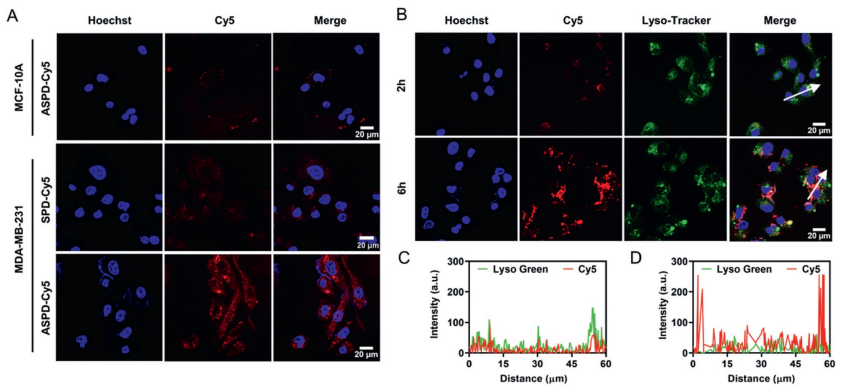


Fig. 2. Cellular uptake and endosomal escape triggered by ASPD. (A) Confocal microscope images of MDA-MB-231 and MCF-10A cells incubated with ASPD-Cy5 (+aptamer), and SPD-Cy5 (-aptamer) at 37 °C for 4 h, respectively. (B) Confocal microscopy images of the subcellular localization of MDA-MB-231 cells incubated with ASPD-Cy5 (ASTD-Cy5 at pH 6.5) for 2 and 6 h, respectively. (C, D) The corresponding diagrams show the fluorescence signal overlap of Lysotracker and ASPD-Cy5 on the arrows drawn in the images. Scale bar: 20 μm. Probe concentration: 200 nmol/L; MB concentration: 200 nmol/L.

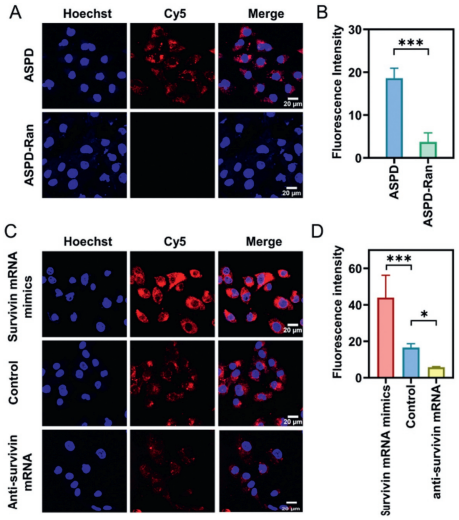


Fig. 3. The specificity of survivin mRNA imaging in MDA-MB-231 cells. (A) Specific imaging and (B) semi-quantitative analysis of survivin mRNA in MDA-MB-231 cells by ASPD (anti-survivin) and ASPD-Ran (anti-random sequence). Probe concentration: 200 nmol/L; MB concentration: 200 nmol/L. (C) Confocal fluorescence imaging and (D) semi-quantitative analysis of survivin mRNA dynamic change levels in MDA-MB-231 cells by the ASPD. Scale bar: 20 μm. Here, the MDA-MB-231 cells were divided into three groups in advance. The first group was transfected with survivin mRNA mimics to increase survivin mRNA expression levels; the second group was an untreated group that served as a control; and the third group was transfected with anti-survivin mRNA to decrease survivin mRNA expression levels. The data are presented as the mean ± SD ($n = 3$). $^{*}P < 0.05$, $^{***}P < 0.001$.

increase, and the maximal intensity was observed at 4 h post-incubation. This verified that ASPD was progressively internalized and recognized intracellular survivin mRNA. To further verify the fluorescence recovery of MB in ASPD is triggered by hybridizing with survivin mRNA rather than self-degradation, ASPD-Ran with a non-targeting control probe was constructed. MDA-MB-231 cells incubated with ASPD exhibited significant Cy5 fluorescence, whereas the ASPD-Ran treated group showed negligible signals (Figs. 3A and B). This confirmed the feasibility of ASPD for recognizing intracellular survivin mRNA.

To evaluate ASPD's ability to detect dynamic mRNA concentrations, survivin mRNA mimics were transfected into MDA-MB-231 cells to simulate a high concentration, and anti-survivin mRNA sequences were transfected to knock down the concentration. The survivin mRNA mimics treated group exhibited significantly stronger fluorescence than the control group, while the anti-survivin mRNA sequences treatment caused weaker fluorescence (Figs. 3C and D). These results demonstrated that ASPD can detect the change in intracellular survivin mRNA level to reflect different stages of tumorigenesis. Overall, ASPD exhibits high specificity and selectivity in recognizing survivin mRNA, underscoring its potential for precise molecular detection in complex biological environments.

The combinative chemo/gene therapeutic potential of ASPD-Dox was evaluated based on survivin mRNA silencing and the chemotherapeutic drug Dox. To assess the efficacy of ASPD, we first examined its gene-silencing effects. Quantitative reverse transcription polymerase chain reaction (qRT-PCR) showed that ASPD caused the largest decrease of survivin mRNA, approximately 70 % compared to the phosphate buffered saline (PBS) control group (Fig. 4A). Then, the western blot analysis revealed that around 72 % of the survivin protein was knocked down by ASPD compared to the control (Figs. 4B and C). Moreover, the results of both qRT-PCR and western blot indicated that ASPD demonstrated a more potent capacity to downregulate survivin compared to ASTD. This finding suggests that the pH-driven ASPD assembly strategy effectively achieved nucleic acid drug delivery and enhanced gene silencing. The biocompatibility of the nanocarrier was first evaluated by testing the ATD and APD without survivin-targeted MB and Dox before measuring the therapeutic effects of ASPD-Dox. CCK-8 assays showed that the cell viability of MDA-MB-231 cells exceeded 95 % after 24 h of incubation with ATD and APD at a high concentration (800 nmol/L) (Fig. 4D), confirming that the nanocarrier is not cytotoxic.

Next, the therapeutic efficacy of ASTD-Dox and ASPD-Dox was examined by cell counting kit-8 (CCK-8) assay. Both ASTD-Dox and ASPD-Dox exhibited dose-dependent cytotoxicity, and ASPD-Dox showed significantly higher cytotoxicity to MDA-MB-231 cells than ASTD-Dox at 600 and 800 nmol/L (Fig. 4E). Furthermore, the therapeutic effects of ASPD-Dox exhibited the strongest cytotoxicity among all groups (Fig. 4F). Then, the calcein-AM and propidium iodide (PI) were used to stain viable and dead cells. The ASPD-Dox group exhibited the highest fluorescence intensity of dead cells (Fig. 4G), consistent with the results of the CCK-8 assay. To further distinguish tumor cells at different apoptotic stages, MDA-MB-231 cells were stained by PI and Annexin V-fluorescein

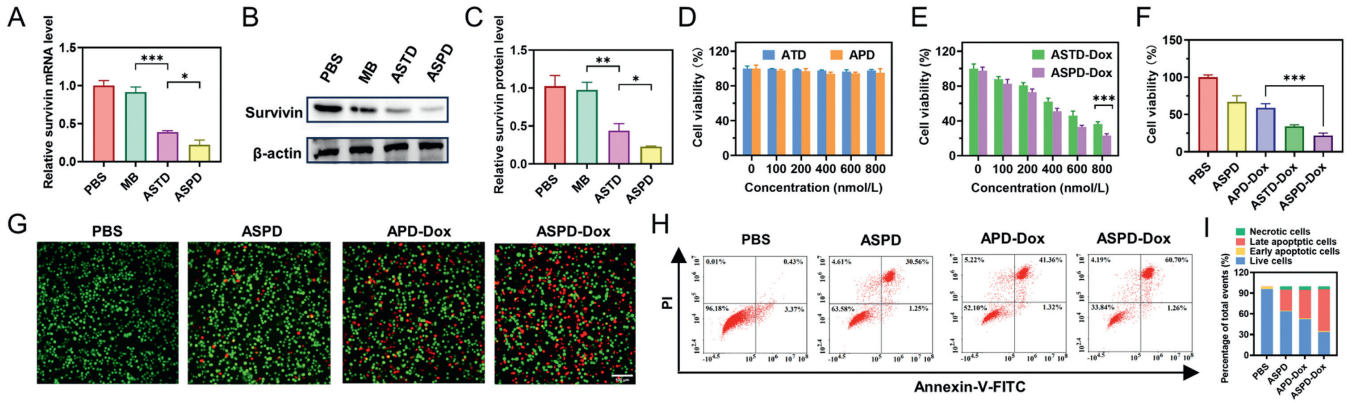


Fig. 4. Gene silencing efficacy of survivin and gene-chemotherapy in MDA-MB-231 cells. (A) qRT-PCR analysis of survivin and (B) Western blot analysis of survivin in MDA-MB-231 cells treated with PBS, MB, ASTD and ASPD for 24 h. (C) Corresponding semi-quantitative analysis of the gray values of the western blot band of the survivin protein by Image J software. (D) Cell viability of MDA-MB-231 cells after coincubation with various concentrations of ATD and APD. (E) Cell viability of MDA-MB-231 cells after coincubation with various concentrations of ASTD-Dox and ASPD-Dox. (F) Cell viability of MDA-MB-231 cells after different treatments at an equivalent probe concentration (800 nmol/L). (G) Fluorescence images of calcein-AM/PI double-stained MDA-MB-231 cells in various groups. Scale bar: 100 μm. (H) Annexin V-FITC/PI staining assay of MDA-MB-231 cells after different treatments. (I) Quantitative analysis of the rate of cell apoptosis in MDA-MB-231 cells treated with various groups. Probe concentration: 800 nmol/L; MB concentration: 800 nmol/L. Data are presented as the mean ± SD ($n = 3$). $^{*}P < 0.05$, $^{**}P < 0.01$, $^{***}P < 0.001$.

isothiocyanate (FITC) after 24 h treatment and analyzed by flow cytometry (Figs. 4H and I). The ASPD-Dox group showed a significantly higher proportion of necrotic and apoptotic cells (~66%) compared to the ASPD group (~36%) and the APD-Dox group (~48%), demonstrating that ASPD-Dox possesses excellent combinative chemo/gene therapeutic effects based on survivin mRNA silencing and chemotherapeutic drug Dox.

In summary, we described a facile strategy to construct a pH-responsive, MB and aptamer-functionalized tetrahedral DNA nanostructure (ASTD), which showed great potential for simultaneous survivin mRNA imaging and combinative chemo/gene therapy. The stimuli-responsive *in situ* DNA assembly mechanism enables ASTD monomers to self-assemble into ASPD on the tumor cell surface upon exposure to the acidic tumor microenvironment. ASPD exhibits enhanced cellular uptake, superior survivin mRNA imaging, and efficient survivin gene silencing. The multifunctional ASPD-Dox exhibited precise detection of survivin mRNA, efficient gene silencing, and controlled release of Dox, achieving excellent combinative antitumor effects. Our nanoplatform showed significant potential for advancing cancer theranostics through its inherent biocompatibility, molecular recognition capabilities, and modular design architecture. We anticipate that this *in situ* stimuli-responsive nanoplatform will inspire further innovations in the field of DNA nanotechnology in cancer research and treatment.

Declaration of competing interest

The authors declare that they have no known competing financial interests or personal relationships that could have appeared to influence the work reported in this paper.

CRediT authorship contribution statement

Mengyue Li: Writing – original draft, Visualization, Methodology, Investigation, Conceptualization. **Yue Zheng:** Visualization, Methodology, Investigation, Conceptualization. **Zhijun Lu:** Methodology. **Yu Yang:** Methodology. **Jiangping Lei:** Methodology. **Yi Teng:** Methodology. **Wanyi Zhou:** Methodology. **Yiman Ge:** Methodology. **Chunhui Wu:** Investigation. **Hong Yang:** Writing – review & editing, Supervision, Conceptualization. **Yiyao Liu:** Writing – review & editing, Supervision, Conceptualization.

Acknowledgments

This research was supported, in part or in whole, by the National Natural Science Foundation of China (Nos. 52372263, 32171395, 12132004, 32471367), the Program for Innovative Fundamental Research Incubation of UESTC (No. Y03023206100226), and the Joint Innovation Fund of Health Commission of Chengdu and Chengdu University of Traditional Chinese Medicine (No. WXLH202403090).

Supplementary materials

Supplementary material associated with this article can be found, in the online version, at doi:10.1016/j.cclet.2025.111541.

References

[1] R. Jia, Y. Wang, W. Ma, et al., Anal. Chem. 94 (2022) 5937–5945.
[2] M. Li, G. Yang, Y. Zheng, et al., J. Nanobiotechnology 21 (2023) 186.
[3] Y. Cai, X. Chen, J. Si, X. Mou, X. Dong, Small 17 (2021) e2103072.
[4] Y. Hou, W. Bu, H. Ai, Z.R. Lu, T. Lammers, Adv. Healthc. Mater. 10 (2021) e2100243.
[5] G. Yang, M. Li, T. Song, et al., Adv. Healthc. Mater. 11 (2022) e2201615.
[6] L. Fan, X. Chong, M. Zhao, et al., Anal. Chem. 93 (2021) 665–670.
[7] Z. Chen, Y. Peng, X. Xie, et al., Theranostics 9 (2019) 5784–5796.
[8] J. Zheng, R. Yang, M. Shi, et al., Chem. Soc. Rev. 44 (2015) 3036–3055.
[9] N. Bidar, F. Oroojalian, B. Baradaran, et al., Trends Analyt. Chem. 131 (2020) 116021.
[10] X. Wu, Y. Zhang, Y. Ding, et al., Adv. Sci. 12 (2025) e2414525.
[11] T. Nie, Z. He, J. Zhu, L. Liu, Y. Chen, Adv. Ther. 3 (2020) 2000016.
[12] I. Nozaki, N. Ishikawa, Y. Miyanari, et al., Bioconjug. Chem. 33 (2022) 2149–2160.
[13] X. Chen, N. Duan, C. Zhang, W. Zhang, J. Cancer. 7 (2016) 314–323.
[14] S.N. Brun, S.L. Markant, L.A. Esparza, et al., Oncogene 34 (2015) 3770–3779.
[15] X. Shen, Q. Ouyang, H. Tan, J. Ouyang, N. Na, Anal. Chem. 95 (2023) 5903–5910.
[16] Y. Yu, L. Zhang, Z. Qin, et al., Adv. Funct. Mater. 33 (2022) 2208797.
[17] H. Wei, F. Li, T. Xue, et al., Bioact. Mater. 28 (2023) 50–60.
[18] T. Nie, Z. He, Y. Zhou, et al., ACS Appl. Mater. Interfaces 11 (2019) 29593–29603.
[19] M. Liu, L. Hao, D. Zhao, J. Li, Y. Lin, ACS Appl. Mater. Interfaces 14 (2022) 38506–38514.
[20] T. Xu, S. Yu, Y. Sun, et al., Small 17 (2021) e2101780.
[21] M. Li, H. Zhang, P. Xiong, et al., J. Control. Release 379 (2025) 452–465.
[22] D. Xiao, Y. Li, T. Tian, et al., ACS Appl. Mater. Interfaces 13 (2021) 6109–6118.
[23] Z. Cai, L. Bai, Q. Li, et al., ACS Nano 18 (2024) 35214–35229.
[24] L. Zhang, Y. Wang, J. Karges, et al., Adv. Mater. 35 (2023) e2210267.
[25] W. Ma, Y. Yang, J. Zhu, et al., Adv. Mater. 34 (2022) e2109609.
[26] M. Zhang, Y. Wen, Z. Huang, et al., Chem. Eng. J. 454 (2023) 140399.
[27] S. Li, T. Zeng, Z. Wu, et al., J. Am. Chem. Soc. 147 (2025) 2168–2181.
[28] D. Xiao, T. Chen, T. Zhang, et al., Chin. Chem. Lett. 35 (2023) 108602.
[29] J. Wang, K. Wang, H. Peng, et al., Anal. Chem. 95 (2023) 4138–4146.
[30] H. Luo, Z. Wang, Q. Mo, et al., ACS Appl. Mater. Interfaces 15 (2023) 33223–33238.
[31] T. Nie, Y. Fang, R. Zhang, et al., Bioact. Mater. 47 (2025) 51–63.
[32] M. Zeraati, D.B. Langley, P. Schofield, et al., Nat. Chem. 10 (2018) 631–637.
[33] M. Debnath, K. Fatma, J. Dash, Angew. Chem. Int. Ed. 58 (2019) 2942–2957.
[34] S. Tao, Y. Run, D. Monchaud, W. Zhang, Trend. Genet. 40 (2024) 853–867.
[35] W. Ma, B. Chen, S. Zou, et al., Anal. Chem. 91 (2019) 12538–12545.